Carbon 178 (2021) 92–102

Contents lists available at ScienceDirect

Carbon

journal homepage: www.elsevier.com/locate/carbon

Research Article

Coherency between thermal and electrical transport of partly reduced graphene paper

Jianshu Gao [a, b, 1], Hamidreza Zobeiri [b, 1], Huan Lin [c], Danmei Xie [a], Yanan Yue [a, **], Xinwei Wang [b, *]

[a] School of Power and Mechanical Engineering, Wuhan University, Wuhan, Hubei, 430072, PR China
[b] Department of Mechanical Engineering, Iowa State University, Ames, IA, 50011, USA
[c] School of Environmental and Municipal Engineering, Qingdao University of Technology, Qingdao, Shandong, 266033, PR China

ARTICLE INFO

Article history:
Received 6 November 2020
Received in revised form
8 February 2021
Accepted 26 February 2021
Available online 13 March 2021

Keywords:
Thermal diffusivity
Electrical conductivity
Thermal annealing
Partly reduced graphene paper

ABSTRACT

By continuously varying the structure of graphene oxide paper (PRGP) using Joule heating annealing, we are able to tune its electrical conductivity (σ) and thermal diffusivity (α) in a very wide range: more than three orders of magnitude for σ (186–503009 S/m) and 10-fold for α (8.31×10^{-7} m^2/s to 9.31×10^{-6} m^2/s). Excellent coherency-linear relationship between σ and α is discovered although they are sustained by different carriers: electrons and phonons. Such coherency exists over two sections: $\sigma > 2 \times 10^4$ S/m, and $10^3 < \sigma < 2 \times 10^4$ S/m. A two-component parallel structure is proposed to interpret the observed discovery. The slope of α~σ relation reflects the ratio of difference in α between the two components over σ of the ordered structure. The intercept of α~σ relation reflects the α of the disordered structure. It is found the α of disordered structure in our PRGP agrees well with that of amorphous carbon. Past work on carbon nanocoil, graphene paper, graphene oxide film, and graphene fiber also reveals linear coherency between α and σ. However, there are no uniform slope and intercept while they are close for similar materials. The parameters of the linear coherency strongly depend on the two structures in the material.

1. Introduction

Graphene consists of sp^2 bonded carbon atoms in the form of a two-dimensional honeycomb lattice [1]. The superior electron mobility and phonon transport make it able to yield exceptional electrical and thermal properties [2]. So far, it is reported that the thermal conductivity of suspended graphene measured at room temperature ranges from 2600 to 5300 W/mK [3,4], and the electrical conductivity is determined to be ~3×10^8 S/m [5]. For various sample synthesis processes, the geometry and assemble mode of graphene sheets are different, which modifies the physical performance of graphene. In addition, carbon atoms could be replaced by other atoms or functional groups, such as graphene oxide sheets, in which the properties of such components may change or even be completely different. The mixture of sp^2 nanograins and amorphous sp^3 networks in graphene oxide sheets result in several orders of magnitude decrease in electrical conductivity (~4×10^{-3} S/m) [6], which is close to an insulating material. At the same time, the lattice defects impede the transport of heat carriers and contribute to a low thermal conductivity of graphene oxide sheet of 0.14–2.87 W/mK [7].

Even if the thermal and electrical conductivity of graphene oxide sheets are quite different from those of graphene sheets, their overall composition structures are similar. In other words, the substitution of carbon atoms with other atoms or functional groups indicates that there may be some potential correlations on physical properties between the graphene oxide sheets and graphene sheets. Deng et al. measured the electrical conductivity and thermal diffusivity of single carbon nanocoils at the same time by using a transient electro-thermal technique [8]. The internal structures of amorphous network and sp^2 grain determine the linear relation between electrical and thermal transport. Liu et al. presented a study of electrical conductivity and thermal conductivity on a giant chemical vapor deposition graphene supported on a polymethyl methacrylate (PMMA) film [9]. The linear correlation between electrical conductivity and thermal conductivity is still valid for graphene with different grain sizes and even in the presence of

* Corresponding author.
** Corresponding author.
E-mail addresses: yyue@whu.edu.cn (Y. Yue), xwang3@iastate.edu (X. Wang).
[1] J. Gao and H. Zobeiri contributed equally to this work.

https://doi.org/10.1016/j.carbon.2021.02.102
0008-6223/

PMMA film. Xie et al. implemented a study to characterize the electrical conductivity and thermal conductivity of packed carbon nanofibers with different densities [10]. The thermal conductivity presents a linear trend versus electrical conductivity for carbon nanofibers. Emmerich investigated the effect of defect concentration on several parameters including thermal conductivity and electrical resistivity (reciprocal of electrical conductivity) in carbon fibers [11]. Even if the defect concentration results in different values of thermal conductivity (22–950 W/mK) and electrical conductivity (71428–833333 S/m), there are linear correlations between thermal conductivity and electrical conductivity among the three types of carbon fibers from different manufacturers. Qiu et al. improved the electrical and thermal transport in carbon nanotube fibers through functionalization and densification [12]. The thermal diffusivity increases from 1.9×10^{-3} m^2/s to 4.7×10^{-3} m^2/s and electrical conductivity is in the range of 24300–65900 S/m. The thermal diffusivity presents a good linear correlation with the electrical conductivity. To better understand the behavior of electrical and thermal transport in carbon-based materials, it is of significance to reveal the mechanism of such a phenomenon.

The electrical and thermal transport in carbon-based materials are affected by the mobility of charge and heat carrier: electrons and phonons. Various types of carrier scattering modes including Umklapp scattering, defect scattering and boundary scattering could contribute to different mean free paths of characteristic carriers [13,14]. For a well prepared polycrystalline graphene film with a grain size of 1–1000 μm [15], the mean free paths of electron and phonon (a few hundreds of nanometers [16]) is much smaller than the grain size. However, the mean free paths of electron and phonon decrease and become close to the grain size as the proportions of defect and boundary are elevated, in which the diffusive transport rather than ballistic transport dominates the mobility of electron and phonon. The grain size has been demonstrated to be effective to regulate the electrical conductivity and thermal conductivity of graphene film [17]. That is, as the mean grain size in graphene is increased from 200 nm to 10 μm, there is a 2–3 folds increase in electrical conductivity and 10 folds improvement in thermal conductivity, which shares a similar evolution trend versus the grain size. However, the correlations between electrical and thermal transport for carbon-based materials with different structural defects are still unclear among published works. This hinders the uncovering of mechanism for electron and phonon transport behavior in carbon-based materials.

In this work, we present an experimental study that uncovers the coherency between thermal diffusivity and electrical conductivity of partly reduced graphene paper (PRGP). Joule heating annealing is applied on the PRGP to reconstruct the internal structure with different annealing currents. The intrinsic electrical conductivity and thermal diffusivity of PRGP are changed in a wide range, which are sensitive to the annealing temperature distribution and are decoupled from the measured overall values in further analyses. The relation between thermal diffusivity and electrical conductivity in PRGP is compared with that of published carbon structures to reveal the in-depth physical behavior based on structure composition.

2. Structure tailoring by current annealing and thermal diffusivity measurement

2.1. Experimental details for annealing and thermal diffusivity measurement

The graphene oxide paper is purchased from the ACS Material Company, which is synthesized from graphite powder by using the modified Hummer's method and vacuum filtration preparation [18]. Due to the amorphous structure and great amounts of functional groups inside, it hinders the transmission of electrons and heat. In order to rebuild the internal structure in graphene oxide paper, a thermal annealing treatment has been introduced as an effective method for removing some functional groups while leaving fewer impurities compared with the chemical reduction treatment [19], which is called PRGP material in this work.

The thermal annealing is implemented on the measured sample by Joule heating while the electrical and thermal properties are obtained from transient electro-thermal technique (TET) characterization. As shown in Fig. 1(a), we design a connection mode for switching between thermal annealing and TET characterization. The sample is cut into a rectangular strip by a razor blade, and it is prepared into a suspended structure with its ends closely attached to electrodes by silver paste as illustrated in Fig. 1(b). The length, width and thickness of the sample are 1.66 mm, 0.24 mm and 12.3 μm, respectively. The sample stage is placed on a cold head with a constant temperature control so that the temperature of electrodes could remain as 300 K during TET measurement. The sample is then placed into a vacuum chamber, where the pressure inside is controlled to be no more than 0.5 mTorr. Therefore convection heat transfer is negligible and the annealing temperature along the sample could be elevated when an annealing current of 1–170 mA is applied by a current source (KEITHLEY 2611A). At a certain heating current, the sample's temperature increases from room temperature and reaches a thermal equilibrium as Joule heating generation dissipates along the sample through conduction and radiation heat transfer. At the same time, some disordered structure in PRGP sample changes into an ordered structure assembly, resulting in the change of resistance and Joule heating power along the sample. The resistance and annealing temperature along the sample evolve gradually until the annealing treatment reaches its final steady state. The thermal annealing is implemented for more than 120 s in order to ensure thermal equilibrium and accomplishment of annealing heating. The voltage evolution during annealing heating is recorded by an oscilloscope (TEKTRONIX DPO3052) as presented in Fig. 1(c). The voltage experiences a rapid decrease at first and then becomes almost stable, which confirms our analyses for this process as mentioned above. Note that the measured voltages here under different annealing currents are useful for further calculation of annealing temperature along the PRGP sample.

The TET technique has been used to successfully measure the thermal properties of various materials [20–23]. After annealing treatment, we allows 40 min for the sample stage to cool down to 300 K. Then TET measurement is conducted to uncover the annealing effect on electrical and thermal behavior. In the TET measurement mode, a step current (0.06–10.6 mA for different cases) is fed through the sample by a current source (KEITHLEY 6221). The TET signal recording uses the same oscilloscope in annealing. The voltage change of the PRGP sample is then monitored as shown in Fig. 1(d). The inset is an enlarged view for one of the TET cycles to reveal its typical voltage change versus time. During TET heating, the temperature of the sample experiences a rapid increase and then reaches a steady state. The generation of Joule heating in the sample dissipates through heat conduction and thermal radiation. Heat convection is negligible due to the high vacuum level in the measurement chamber. The temperature evolution is sensitive to the equilibrium between heat generation and heat dissipation. A one-dimensional thermal transport model is applicable to the sample. The normalized average temperature rise, defined as $T^* = [T(t) - T_0]/[T_\infty - T_0]$, is given as [24].

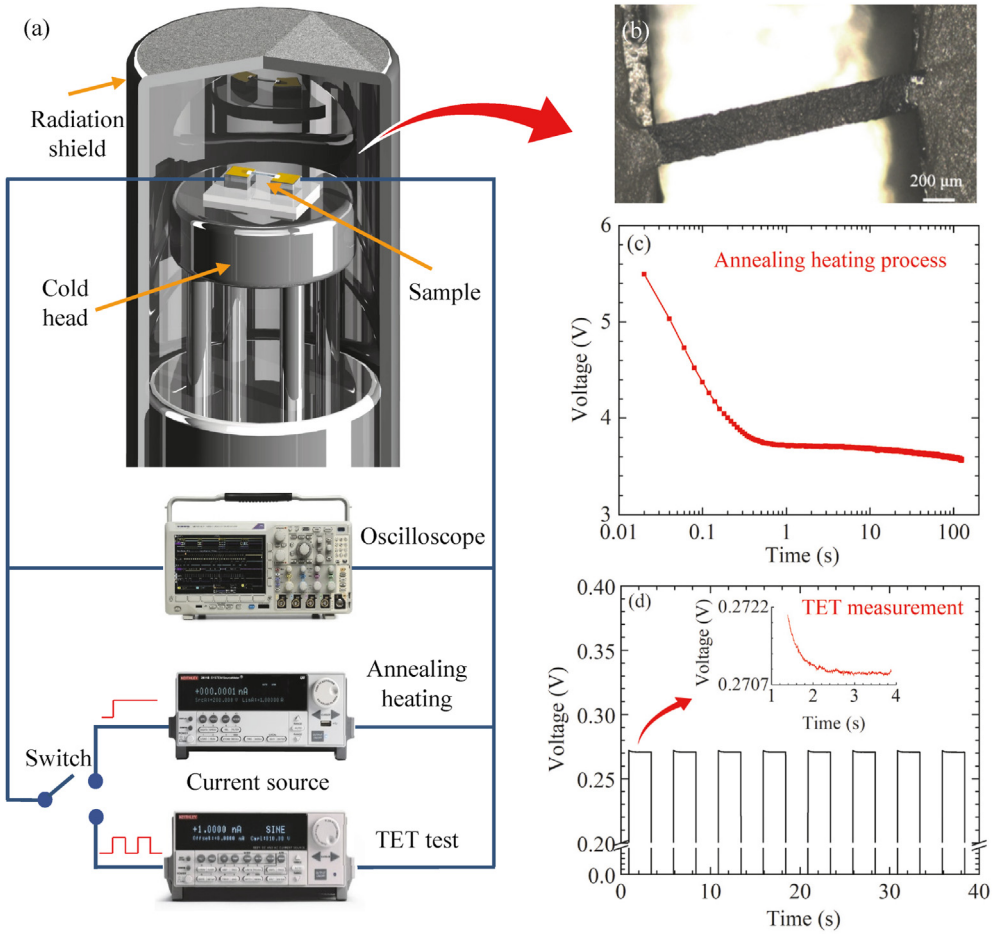

Fig. 1. (a) Schematic setup for annealing heating and TET characterization on the PRGP sample. (b) Optical image of the suspended PRGP sample. (c) Typical voltage evolution with respect to time during annealing heating process. (d) TET signal of the PRGP. The inset presents the enlarged view for one of the measurement cycles. . (A colour version of this figure can be viewed online.)

$$T^* = \frac{48}{\pi^4}\sum_{m=1}^{\infty}\frac{1-(-1)^m}{m^2}\frac{1-\exp[-m^2\pi^2\alpha_{eff}t/L^2]}{m^2} \quad (1)$$

where t is the time, L the sample length and α_{eff} the effective thermal diffusivity. Note that the radiation effect has not been decoupled from α_{eff} here. It will be taken into account in calculating the intrinsic thermal diffusivity. Among the slight temperature rise induced from heating current in TET measurement, the temperature coefficient of resistance for PRGP sample could be assumed constant. The sample resistance is sensitive to temperature so that the normalized temperature rise can be obtained from voltage variation as recorded in oscilloscope, which is described as $U^* = [U(t) - U_0]/[U_\infty - U_0]$, where $U(t)$, U_0 and U_1 are the voltage at time t, initial and steady-states, respectively. In Eq. (1), the normalized temperature rise, equal to the value of normalized voltage variation, is used for determining the thermal diffusivity of the PRGP sample.

2.2. Transient behavior under different annealing level

The evolution of electrical resistance with respect to time during annealing heating is presented in Fig. 2(a) at different heating currents. Under the effect of Joule heating, the electrical resistance first decreases rapidly, and then moves towards a stable value as the annealing process continues. The electrical resistance at steady state is smaller than the initial one, some of which is irreversible even after the heating is done. It is attributed to the negative resistance-temperature coefficient of PRGP sample and structure improvement during annealing process. The changing rate of resistance during annealing, defined as the derivative of resistance versus time, decreases with the annealing time. The electrical resistance becomes saturated for an improved crystallinity as the time is extended. The annealing heating process could be considered consisting of three processes. Within the annealing heating procedure, the resistance first decreases with little structure change as the temperature is elevated. This is introduced by some physical modes including the rotation and the thermal expansion of sp^2 grains. Second, the resistance continues to decrease under the combined effects of temperature rise and the internal structure annealing. The reconstruction of crystallinity and bond connection in PRGP sample contribute to the change of intrinsic electrical resistance and thermal properties. Under a certain annealing current, the Joule heating and heat dissipation keep evolving and establish a new temperature profile along the PRGP sample. Third, with the annealing moves forward, the electrical resistance gradually transfers into a stable value as the thermal equilibrium is established. For different annealing currents, the resistance at higher currents reaches a steady state within a shorter time compared with that at low annealing current. For example, it takes 1 s for the resistance of the PRGP sample to stabilize at annealing

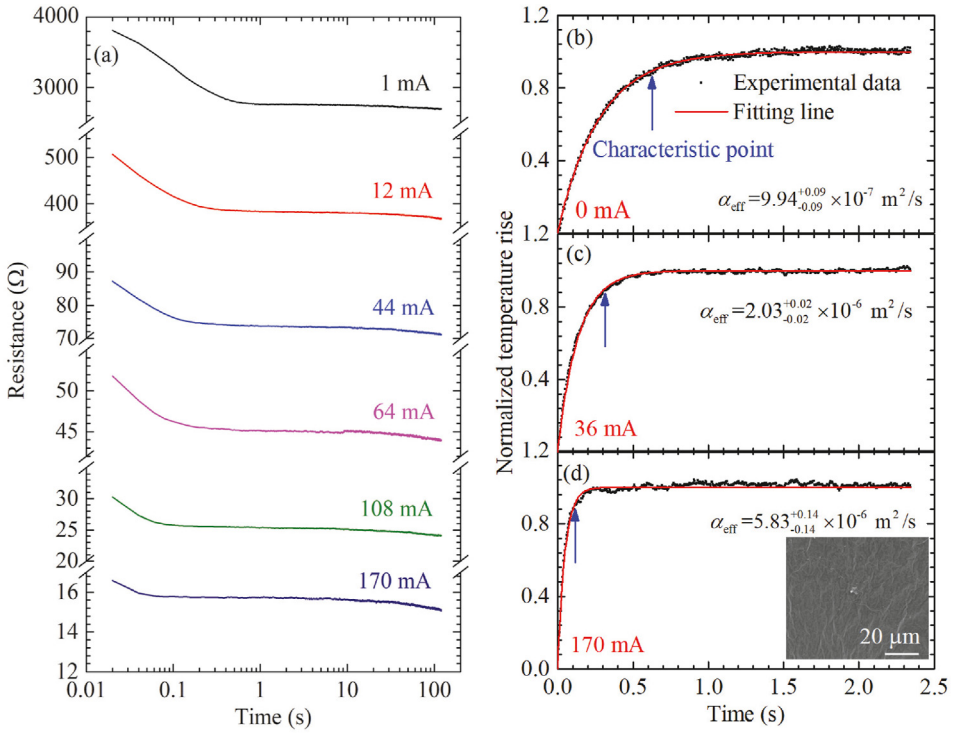

Fig. 2. (a) Resistance change of PRGP sample in annealing heating process with different heating currents. The effective thermal diffusivity calculated from the normalized temperature rise by using the TET technique after annealing treatment for heating currents of (b) 0 mA (the original sample), (c) 36 mA and (d) 170 mA, respectively. The inset in figure d shows the SEM image of the PRGP sample. (A colour version of this figure can be viewed online.)

current of 1 mA while that time is less than 0.1 s for 170 mA. The disordered structure takes large proportion in graphene oxide paper, which is dramatically modified as the annealing treatment is implemented. It is speculated that the crystallinity reconstruction effect for the case of 170 mA may not be as fierce as that of 1 mA. The amorphous structure takes a large proportion in graphene oxide paper, which is dramatically modified as the annealing treatment is implemented. In the annealing process, when the current is higher, the annealing will take a shorter time since the previous annealing has finished reforming some structures.

When the sample temperature returns to 300 K after annealing, the TET technique is implemented to determine the thermal diffusivity of PRGP sample with diverse crystallinity reconstructions. Fig. 2(b–d) show the normalized temperature rise versus time for different annealing currents. The normalized temperature rise has a similar trend of increasing with time. However, the characteristic point (0.87 for T^*) differs for various annealing currents. For the original sample, the characteristic point occurs at 0.57 s, while the characteristic point after 170 mA annealing occurs at 0.10 s. It reveals that the thermal diffusivity of PRGP sample at 170 mA is increased significantly after the annealing treatment, which is much larger than that of 0 mA and 36 mA. The corresponding effective thermal diffusivity is determined to be $9.94^{+0.09}_{-0.09}\times\ 10^{-7}$ m^2/s, $2.03^{+0.02}_{-0.02}\times10^{-6}$ m^2/s and $5.83^{+0.14}_{-0.14}\times 10^{-6}$ m^2/s for PRGP sample after annealing with current of 0 mA, 36 mA and 170 mA, respectively. The uncertainty of thermal diffusivity measurement is evaluated from the least square fitting method with 95% confidence interval. Xie et al. [25] has employed the TET technique to characterize the thermal diffusivity and thermal conductivity on PRGP materials. The thermal diffusivity of their PRGP sample is calculated to be 1.56–2.63 $\times\ 10^{-6}$ m^2/s at 300 K, which is consistent with our measurement results. The scanning electron microscope (SEM) image is shown in the inset of Fig. 2(d). Even if there are some wrinkled structures on the surface, the PRGP film presents a uniform structure without any voids.

Fig. 3(a) illustrates the variation of electrical resistance for the PRGP sample in thermal annealing and after annealing treatment. The electrical resistance in annealing process (R_{IA}) is determined from steady state voltage while the resistance after annealing (R_{AA}) is calculated from TET technique as the sample temperature returns to 300 K. The R_{IA} decreases from 4532 Ω to 15 Ω as the annealing power increases from 0 W to 0.44 W. Among the same annealing power, the R_{AA} decreases from 4532 Ω to 20 Ω. The decrease by more than two orders of magnitude is ascribed to the improvement of internal ordered structure in PRGP sample by thermal annealing. Under the same annealing power, it is found that the R_{IA} is smaller than R_{AA} due to the negative resistance-temperature coefficient of PRGP sample [26]. The resistance change percentage in and after annealing is also summarized in Fig. 3(a). It is observed that the resistance change percentage versus annealing power first increases and then decreases, rather than a constant. The maximum value of 58% appears when the annealing power is 0.045 W. The resistance change percentage is sensitive to effects of the structure reconstruction in thermal annealing and the negative resistance-temperature coefficient of PRGP sample.

The results of α_{eff} after different power annealing are summarized as shown in Fig. 3(b). The α_{eff} increases from $9.94^{+0.09}_{-0.09}\times\ 10^{-7}$ m^2/sto $5.83^{+0.14}_{-0.14}\times 10^{-6}$ m^2/s among the range of annealing power up to 0.44 W. The increase by 487% is attributed to the transformation of disordered structure into ordered structure, which is much more obvious for a higher annealing power. The annealing treatment also removes some oxygen-containing functional groups in sp^3 carbon bonds in the atomic network of the PRGP sample, leading to enhancement of thermal diffusivity. It is reported that for annealing temperatures higher than 1773 K, the lattice fringes straighten up, and single rings begin to appear [27–29]. As

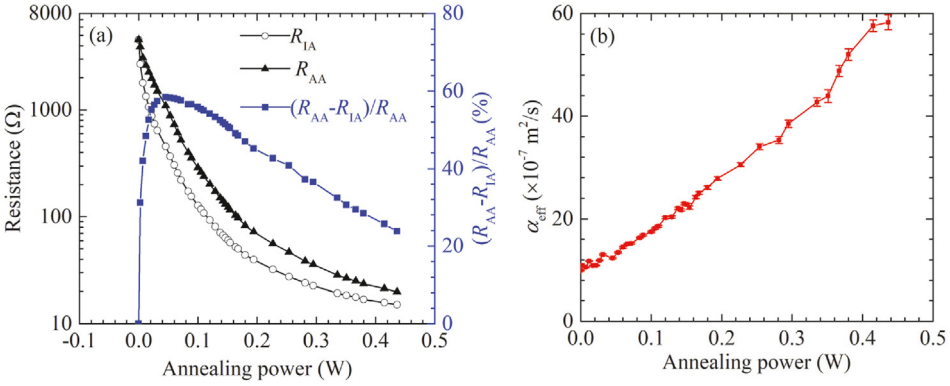

Fig. 3. (a) Electrical resistance of PRGP sample with respect to annealing power in annealing process and after thermal annealing (300 K). (b) Measured effective thermal diffusivity of PRGP sample after the treatment with different annealing powers. . (A colour version of this figure can be viewed online.)

the annealing temperature is elevated to 2273 K, the open edges are represented by the double-loop form. For a higher annealing temperature (2773–3073 K), the lattice fringes are getting straighter in a mode of covering more number of layers and the absence of open edges. With the increased annealing power, a higher annealing temperature along the PRGP sample is created, which improves the internal sp^2 carbon bond structure and thermal diffusivity.

2.3. Determination of annealing temperature profile and intrinsic electrical conductivity and thermal diffusivity

Thermal annealing is implemented on the PRGP sample in a two-point setup. The heat conduction and thermal radiation balance the Joule heat generation in the sample, resulting a non-uniform annealing temperature profile and physical property profile along the one-dimensional system. In other words, the electrical resistance and thermal diffusivity determined above represent the average of PRGP sample that has a property variation along the axial direction due to the annealing temperature distribution. To reveal the correlation between the intrinsic thermal and electrical transport in PRGP sample, the electrical and thermal behaviors at a specific annealing temperature need to be determined precisely. Therefore, it is of significance to calculate the real annealing temperature profile with consideration of the intrinsic thermal and electrical properties. Below we describe the methods to determine intrinsic thermal diffusivity and electrical resistivity of the sample specifically annealed at a given temperature.

As shown by the schematic in Fig. 4(a), in the first annealing heating, first of all, the electrical resistivity is assumed constant along the sample and can be calculated based on the overall sample's electrical resistance. Using this assumed electrical resistivity and the known heating current, we calculate the temperature distribution along the sample. The highest temperature (at the middle point of the sample) is T_1. Now we consider the distribution of the electrical resistivity along the sample, and local electrical resistivity at the sample's middle point is ρ_1. With the fact that T_1 will not differ a lot from the T_0 under the first low current annealing, the electrical resistivity at other locations of the sample is assumed to vary linearly with the local temperature. Based on the calculated temperature distribution, the value of ρ_1 is determined by comparing the sum of the calculated electrical resistance at each location and the measured overall electrical resistance. This newly calculated electrical resistivity distribution will be used to calculate the temperature distribution again to repeat the above process until the temperature profile changes by <0.5% between two consecutive calculations. For the second annealing current heating, the same treatment is conducted, but the electrical resistivity and temperature relation for $T < T_1$ use the result obtained by the last time annealing processing. For other annealing processes, similar calculation strategies are applied to establish the real annealing temperature profiles.

Note that the radiation heat transfer is taken into account with an emissivity of 1 during the entire calculation. At this time, the real annealing temperature along the PRGP sample is determined, as presented in Fig. 4(b). The trend of annealing temperature profile is consistent with the previous speculations that the annealing temperature is non-uniform. Due to the higher annealing temperature, the annealing effect at the midpoint could be better than that at the sample end. The highest annealing temperature is up to 2119 K under the annealing current of 170 mA. The calculation of real annealing temperature profile is beneficial for further analyses to uncover the correlation and mechanism of electrical and thermal properties of PRGP sample.

Similar to the calculation strategy in real annealing temperature profile, the intrinsic electrical conductivity (σ_{int}) and intrinsic thermal diffusivity (α_{int}) are determined by combining the measured overall electrical resistance and the effective thermal diffusivity in TET tests. As shown in Fig. 5(a), the σ_{int} increases from 186 S/m to 5.03 × 10^5 S/m when the annealing temperature is increased to 2119 K σ_{int} experiences a slow increase below 1300 K, and then increases rapidly after temperature exceeding 1300 K. The initial change (in red region) is presented in the inset of Fig. 5(a). The absolute value of σ_{int} increases by three orders of magnitude with the annealing temperature. In Fig. 5(b), α_{int} is elevated from 8.31 × 10^{-7} m^2/s to 9.31 × 10^{-6} m^2/s with the annealing temperature. The enhancement by 2703 folds for σ_{int} and 10 folds for α_{int} is ascribed to the change in internal structure induced by thermal annealing. The disordered structure in PRGP sample suppresses the electrical conductivity and thermal diffusivity. Lin et al. [30] prepared a pristine graphene oxide film with an electrical conductivity of 0.01 S/m and an enhancement by ~2.8 × 10^5 folds is observed for the sample after thermal annealing. The removal of oxygenated functional groups in reduced graphene paper facilitates the electron mobility compared to the pristine materials. Renteria et al. [31] employed a laser flash method to characterize the thermal properties of graphene oxide film and that after thermal annealing. The thermal conductivity of graphene oxide film is determined to be 2.9 W/mK, which was increased to 61 W/mK after thermal annealing. Assuming the specific heat capacity and density equivalent to that of graphite as 709 J/kgK and 2210 kg/m^3 [32], the thermal diffusivity is determined to be 1.85 × 10^{-6} m^2/s for graphene oxide paper and 4.08 × 10^{-5} m^2/s for reduced graphene paper. The increase by 22 folds in thermal diffusivity is in the same order of magnitude as our results.

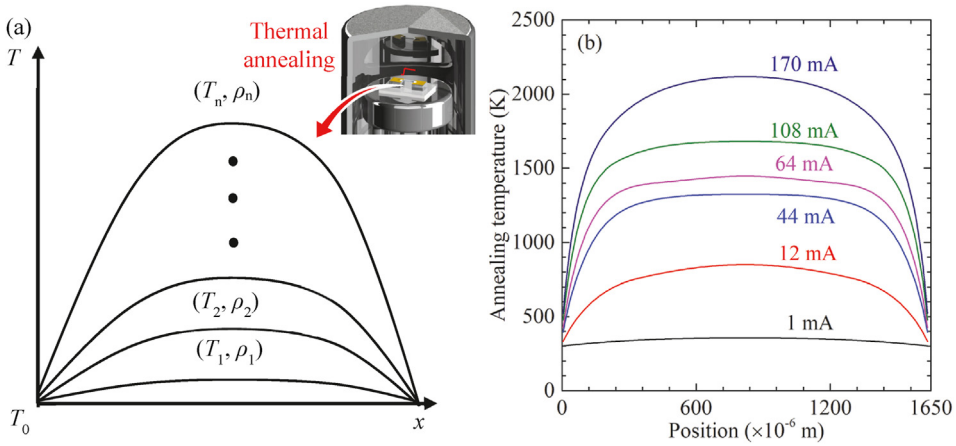

Fig. 4. (a) Schematic of annealing temperature profiles along the sample under Joule heating. (b) Real annealing temperature profile along the PRGP sample at selected heating currents. (A colour version of this figure can be viewed online.)

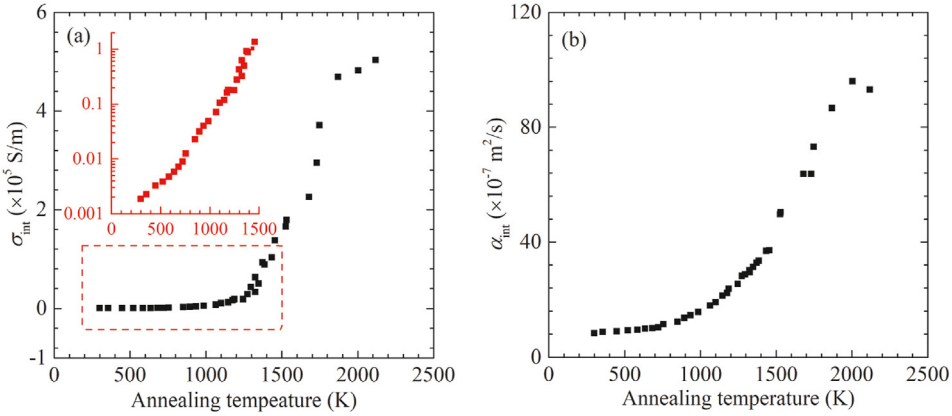

Fig. 5. (a) Intrinsic electrical conductivity and (b) intrinsic thermal diffusivity of PRGP sample annealed at different temperatures. The inset in Fig. (a) shows the initial electrical conductivity change, which is small in absolute value, but is very large in terms of relative change (~3 orders of magnitude). (A colour version of this figure can be viewed online.)

2.4. Structure evolution characterized by Raman spectrum

Raman spectroscopy is applied to study how the thermal annealing changes the internal structure of PRGP by scanning the position from sample end to middle point [see Fig. 6(a-b)], in which the two-dimensional map is plotted with different colors according to the measured Raman intensity. The Raman spectrum of PRGP is collected under an excitation laser of 532 nm. Details of our Raman measurement and setup have been given in our previous works [33–35]. The PRGP exhibits two typical peaks at 1350 cm^{-1} and 1570 cm^{-1}, corresponding to the D peak and G peak. It is observed that the separation between D peak and G peak becomes pronounced as the position shifts from sample end to middle point (increased annealing temperature). During this process, the intensity of D peak decreases while the intensity of G peak increases dramatically. This indicates the rare defects and good crystallinity for the position near the middle point of the PRGP sample. As shown in Fig. 6(c), the area ratio of D peak over G peak (A_D/A_G) decreases from 1.19 at the sample end to 0.20 at the middle point. The annealing treatment reduces the amount of sp^3 carbon bond and facilitates the formation of sp^2 carbon bond. For annealing heating on a two-point setup, the annealing power introduces a non-uniform annealing temperature along the PRGP sample. The PRGP transforms from a disordered structure (sample end) to a more ordered material (middle point) with a higher annealing temperature, resulting in a non-uniform structural modification. These results also demonstrate the non-uniform effect on electrical and thermal properties along the PRGP sample.

3. Coherency between thermal and electrical transport

Using the values of intrinsic electrical and thermal transport properties after annealing at different temperatures, the correlation between α_{int} and σ_{int} is presented in Fig. 7(a) α_{int} experiences a rapid increase and then exhibits a linear trend with respect to σ_{int}. The linear relation between electrical and thermal properties in PRGP is similar to the Wiedemann-Franz law in metals, but is completely different in physical mechanisms. In metals, free electrons sustain both electrical and major thermal conduction. However, the charge carriers in PRGP are electrons while the heat carriers are electrons and phonons, mostly phonons. The presence of localized nanograins and amorphous networks affects the electrical and thermal transport in PRGP. For electrical transport, it is reported that the electron mobility in graphene is sensitive to dislocation density, disorder of grain boundary, grain size and interconnected network assembly [36,37]. When there are some chemical species such as oxygen and hydroxyl inside, they facilitate more electron scattering and reduce the electron's mean free path [38]. The increased defect and grain boundary structure result in fierce phonon scattering and suppress the thermal transport [39].

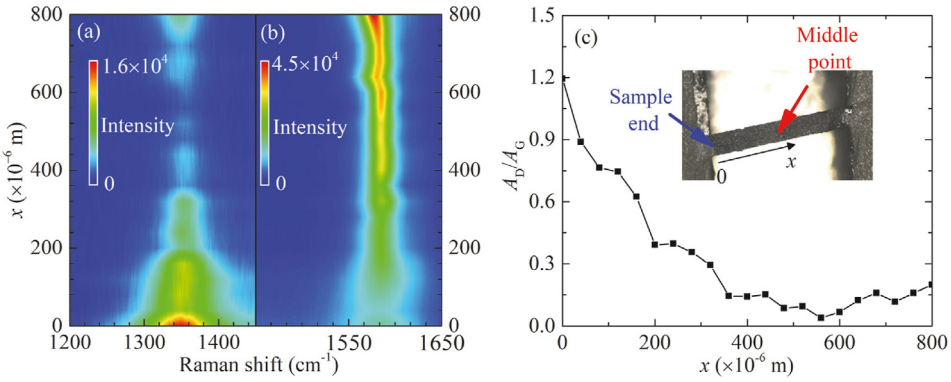

Fig. 6. Two-dimensional contour map to demonstrate the evolution of (a) D peak and (b) G peak in Raman shift versus the distance from the sample end. (c) Ratio of A_D/A_G in Raman signal versus the distance from the sample end. The coordinate x is defined in the inset of figure (c). (A colour version of this figure can be viewed online.)

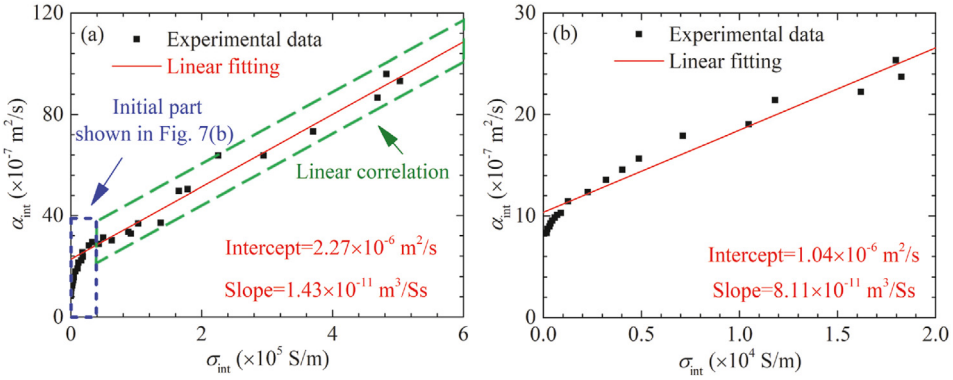

Fig. 7. (a) The intrinsic thermal diffusivity versus intrinsic electrical conductivity. The linear fitting is applied to determine the intercept and slope. (b) The enlarged correlation between intrinsic thermal diffusivity and intrinsic electrical conductivity in initial region (blue region) in (a). (A colour version of this figure can be viewed online.)

The electrical and thermal properties of disordered structure are quite different from that of ordered structure. The transformation from amorphous sp^3 network to sp^2 grains modifies the electrical and thermal transport in PRGP [40,41]. Therefore, the mixture of disordered structure and ordered one could create different forms of electrical and thermal transport in PRGP due to the modification by annealing temperatures.

The PRGP studied in our work possesses layered structure assembled by disordered structure and ordered structure. In each combination layer, the ordered structure are connected to the adjacent disordered structure or ordered one. The adjacent grain planes of ordered structure and disordered structure are parallel to each other, forming a layered structure in PRGP. Here, the electrical conductivity and thermal diffusivity of disordered structure in PRGP are defined as σ_d and α_d, while those of ordered one are σ_g and α_g, respectively. Even though the properties of ordered structure are anisotropic within the layer and between the layers, the grain planes of ordered structure and disordered structure are parallel. The linear combination of electrical and thermal properties for ordered structure and disordered structure could be described as [8].

$$\alpha_{real} = \gamma\alpha_d + (1-\gamma)\alpha_g \;\; \sigma_{real} = \gamma\sigma_d + (1-\gamma)\sigma_g \tag{2}$$

where γ is the volumetric fraction of the disordered structure in PRGP. The subscript "d" and "g" are for disordered and ordered structure. The value of γ between 0 and 1 is sensitive to the temperature in annealing heating. That is, γ decreases versus annealing temperature because of improvement of internal structure. From Eq. (2), the correlation between electrical conductivity and thermal diffusivity is then expressed as

$$\alpha_{real} = A\sigma_{real} + B \tag{3}$$

where the slope $A = (\alpha_d - \alpha_g)/(\sigma_d - \sigma_g)$ and intercept $B = (\sigma_d\alpha_g - \sigma_g\alpha_d)/(\sigma_d - \sigma_g)$. Thermal annealing introduces internal structure transform from disordered structure to ordered structure. During this process, the volumetric fraction of these two components is changed but there is slight influence on each one's electrical conductivity and thermal diffusivity. Therefore, the value of A and B remains constant during thermal annealing.

As shown in Fig. 7(a), the trend between the α_{int} and σ_{int} is separated into two sections including the initial part (blue region) and the linear correlation section (in green region). In the initial part ($\sigma_{int} < 2 \times 10^4$ S/m), the discrepancy of electrical and thermal transport of disordered structure and ordered structure in PGRP contributes to a rapid increase of α_{int}. The electron transport requires a connected conductive network to establish an electron transport channel. In the original PRGP sample, the disordered structure dominates the layer structure, which is close to an electrically non-conductive material. As a consequence, the electron conduction channel could not be well established until the ordered structures are connected to each other under the effect of thermal annealing. However, even if the electrical channel is not fully established yet, heat can still be transferred between the disordered structure and the ordered structure through lattice vibration. Therefore in the beginning, any improvement in connection of the ordered structure will result in a small absolute increase of

electrical conductivity, while the increase of relative value is significant in establishing the electrical channels.

As the connected network of ordered structure is gradually established, the absolute enhancement of electrical conductivity becomes more pronounced. In the linear correlation mode (σ_{int} exceeds 2×10^4 S/m), the electrical and thermal transport properties are analyzed by physics mechanisms of two-composite mixture as given in Eq. (3). The effect of thermal annealing on PRGP changes the volumetric fraction of disordered structure and the ordered structure. The correlation between α_{int} and σ_{int} is described in a linear form with a slope of $(\alpha_d - \alpha_g)/(\sigma_d - \sigma_g)$ and an intercept of $(\sigma_d\alpha_g - \sigma_g\alpha_d)/(\sigma_d - \sigma_g)$. For the disordered structure, σ_d is close to zero while α_d is still non-trivial. The slope is then in the form of $(\alpha_d - \alpha_g)/(-\sigma_g)$ and the intercept is α_d. As presented in Fig. 7(a), linear fitting is applied to determine the values of slope and intercept in linear correlation mode by using the least square method. The intercept is calculated to be 2.27×10^{-6} m^2/s and the slope is 1.43×10^{-11} m^3/S, which indicates the thermal diffusivity of the disordered structure in PRGP is 2.27×10^{-6} m^2/s. Dias et al. [42] has conducted thermo-optical characterization of hydrogenated amorphous carbon thin films. The thermal diffusivity at room temperature is evaluated to be $0.34–1.40 \times 10^{-6}$ m^2/s for different deposition times. These results agree well with the thermal diffusivity of the disordered structure determined in our work.

For the initial section shown in Fig. 7(a) that has very fast relative increase of electrical conductivity, we also plot out the thermal diffusivity change versus the electrical conductivity change and show the results in Fig. 7(b). A linear relation is also observed between the thermal diffusivity and electrical conductivity for $\sigma_{int} > 1 \times 10^3$ S/m. The linear fitting of this section data gives an intercept of 1.04×10^{-6} m^2/s and a slope of 8.11×10^{-11} m^3/S. As mentioned above, the network of electrical channel is in the stage of gradual establishment for initial evolution mode. The intercept here is not valid for disordered structure in PRGP but is in the same order of magnitude as that in Fig. 7(a). For the data section with $\sigma_{int} < 1 \times 10^3$ S/m, since the thermal diffusivity changes very little, linear fitting will make less physical sense and is not conducted here.

4. Coherency physics and extension to other carbon structures

In PRGP, α_{int} increases by an order of magnitude while σ_{int} increases by three orders of magnitude. The phenomenon could be related to the fact that the electron transport across the grain boundary is more impeded than phonons [43]. The electron scattering at the grain boundary of the ordered structure and disordered one is different from phonon scattering. The electrical conductivity is ascribed to the quantum mechanical scattering of electrons across all grain boundaries in PRGP. The electrons reflected from the grain boundary have no charge transport contribution. However, the reflected phonons at the grain boundary will exchange energy with phonons at the other side of the boundary and facilitate thermal transport [44]. Even though there is a wide range of values in electrical and thermal transport properties due to the different levels of crystallinity, the linear relation between electrical conductivity and thermal diffusivity is still valid in PRGP. The volumetric fractions of the disordered structure and ordered one are different in such a two-composite material, revealing that the value of electrical and thermal transport properties would vary between the two extremes. In addition, the coherency between the electrical conductivity and thermal diffusivity is not only valid for PRGP, but it also exists for many two-composite materials with structure arrangement parallel to the directions of electrical and thermal transport [45,46]. These include amongst other carbon materials such as carbon nanocoil, graphene paper, graphene fiber, graphene oxide film, and so on. The overall electrical and thermal transport properties of the two-composite material are sensitive to the combined behavior of electron and phonon transport in layered structure.

To investigate the robust and generalized correlation in other carbon materials, the electrical and thermal transport properties reported in literatures [47–50] are collected and shown in Fig. 8(a–d). The linear fitting (red and blue lines) is applied to uncover the correlation between electrical conductivity and thermal diffusivity. It is observed that the thermal diffusivity presents a very good linear increasing trend with the increased electrical conductivity in carbon nanocoils, graphene papers, graphene fibers and graphene oxide film, in which the directions of electrical and thermal transport of interest are parallel to the internal structure arrangement direction. The electrical conductivity has a wide range of variation from ~10^3 S/m to ~10^6 S/m while thermal diffusivity is within the range of 10^{-7}-10^{-3} m^2/s. To reveal the underlying mechanism in electrical and thermal transport, the determined intercepts and slopes are summarized in Table 1. The intercept and slope in two-composite system is described in the form of α_d and $(\alpha_d - \alpha_g)/(-\sigma_g)$ by assuming the electrical conductivity of disordered structure close to zero. The microscopic structure in carbon materials contributes to a difference of disordered structure and ordered structure, resulting in a discrepancy in electrical and thermal transport. A large value of intercept indicates a high thermal diffusivity in disordered structure. If α_g is much larger than α_d (usually valid in carbon-based materials), the slope becomes an approximation of the ratio of thermal diffusivity and electrical conductivity of ordered structure (α_g/σ_g). Therefore, the intercept and slope of linear fitting between electrical conductivity and thermal diffusivity for two different materials would be in a close value if these two materials share similar disordered structure and similar ordered structure, which generally occurs in materials with the similar synthesis method.

Among the same materials such as carbon nanocoils, the intercepts determined for two carbon nanocoils are 7.88×10^{-7} m^2/s and 1.12×10^{-7} m^2/s, along with the slopes calculated as 5.13×10^{-11} m^3/S and 9.19×10^{-11} m^3/S. It means that the thermal diffusivity of disordered structure and the α_g/σ_g are in close values in carbon nanocoil. This is reasonable since the internal assembly (disordered structure and ordered structure) of carbon nanocoil is similar under the same synthesis method. The similarity is also observed for graphene paper, graphene fiber with the same sample preparation. Compared with our PRGP sample, the results of graphene oxide film is similar in slope but much different in intercept. It is ascribed to the similar α_g/σ_g in sound ordered structure and the discrepancy in disordered structure with different synthesis methods [51,52]. Nirmalraj et al. characterized the thickness dependence of electrical properties of individual graphene strip [53]. The electrical conductivity of monolayer graphene is determined to be ~1×10^8 S/m. Wang et al. studied the thermal properties of suspended monolayer graphene [54]. They revealed that the thermal conductivity of pristine monolayer graphene is 2000–2200 W/mK and the corresponding thermal diffusivity is $1.28–1.40 \times 10^{-3}$ m^2/s. The α_g/σ_g of monolayer graphene is estimated as $1.28–1.40 \times 10^{-11}$ m^3/S. The result is quite close to the slope of our PRGP sample, which uncovers the structure reconstruction of PRGP in thermal annealing toward pristine graphene.

For different materials, it is difficult to compare the values of slope and intercept with each other even if carbon element is the main component. The discrepancy in intercept and slope is attributed to the sample difference and measurement uncertainty. The complex mixture of sp^3 and sp^2 carbon structure contributes to specific slope and intercept among different materials, in which the

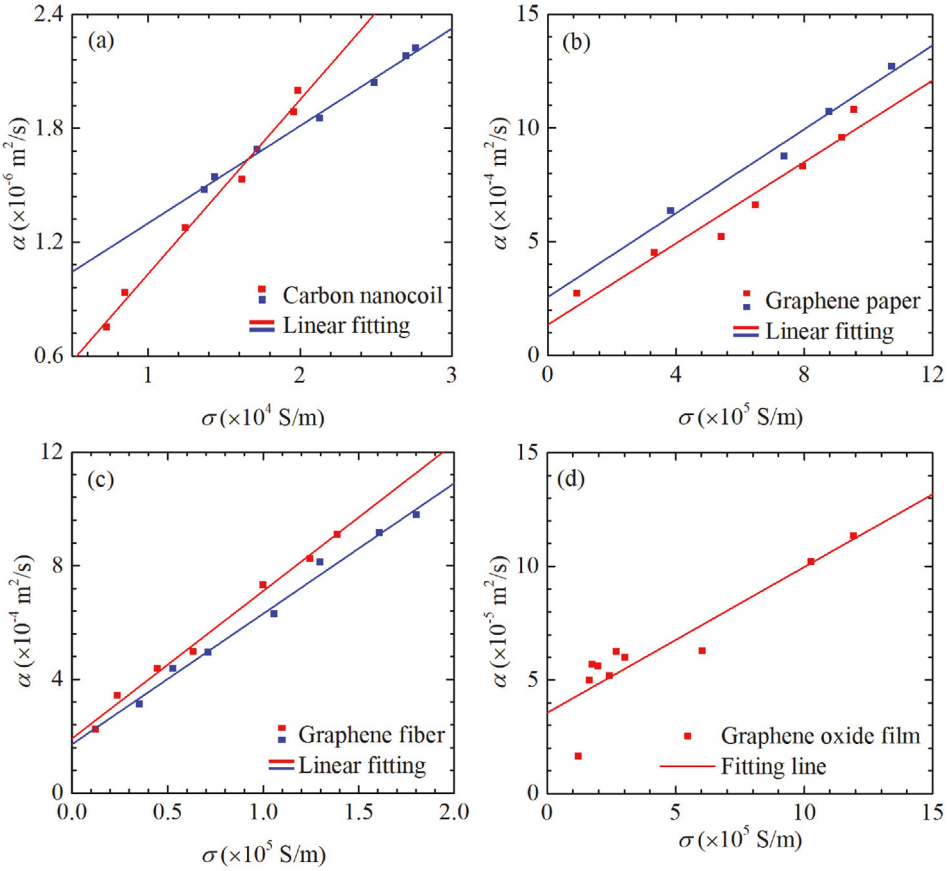

Fig. 8. The linear correlations between electrical conductivity and thermal diffusivity in (a) carbon nanocoils, (b) graphene papers, (c) graphene fibers and (d) graphene oxide film. (A colour version of this figure can be viewed online.)

Table 1
The intercepts and slopes in linear fitting between the electrical conductivity and thermal diffusivity in different carbon structures.

Materials	Intercept (m^2/s)	Slope (m^3/Ss)
Carbon nanocoil [47]	7.88×10^{-7}	5.13×10^{-11}
Carbon nanocoil [47]	1.12×10^{-7}	9.19×10^{-11}
Graphene paper [48]	1.37×10^{-4}	8.93×10^{-10}
Graphene paper [48]	2.57×10^{-4}	9.22×10^{-10}
Graphene fiber from LGGO [49]	1.91×10^{-4}	5.19×10^{-9}
Optimized graphene fiber [49]	1.71×10^{-4}	4.59×10^{-9}
Graphene oxide film [50]	3.56×10^{-5}	6.41×10^{-11}
This work	2.27×10^{-6}	1.43×10^{-11}

linear correlation of electrical and thermal transport is still valid. The initial structure changing part in PRGP (slow α increase and fast σ increase) may not be found in other carbon materials if their electrical conduction channel has been established in a good initial structure arrangement. For our observed linear relation between thermal diffusivity and electrical conductivity, some speculations have been proposed in the past to explain such relation for carbon fibers by similar electron and phonon scattering by defects [55]. In our studied samples, with the annealing-induced structure improvement, the free electron population could also be improved, which will put another effect on electrical conductivity increase. This will make the relation between thermal diffusivity and electrical conductivity non-linear. Therefore, the structure composition effect is more physically reasonable to explain the observed linear relation between thermal diffusivity and electrical conductivity.

5. Conclusions

In conclusion, we reveal the coherency between thermal diffusivity and electrical conductivity in PRGP with Joule heating annealing that reconstructs the internal structure. The annealing temperature profiles at different annealing currents were calculated with rigorous physics consideration, and the highest point reached 2119 K. The α_{int} and σ_{int} of PRGP at different annealing temperatures were extracted from the overall values. It was found that σ_{int} was increased by 2703 folds and α_{int} by more than 10 folds. The electrical transport channel was gradually established in initial evolution of annealing so that the electrical conductivity increases by three orders of magnitude. Excellent coherency—linear relationship existed between α_{int} and σ_{int} although they were controlled by different physical mechanisms. The thermal diffusivity of disordered structure in PRGP was 2.27×10^{-6} m^2/s as determined from the intercept of α_{int}~σ_{int} relation. The linear coherency between thermal diffusivity and electrical conductivity was also valid for other carbon materials with structure arrangement direction parallel to the directions of electrical and thermal transport. However, there are no uniform constants for the linear coherency for all carbon materials, which is sensitive to the structure composition in the material. This work provides a strategy for designing thermal transport and electrical materials. The electrical and thermal properties of carbon materials could be changed by varying the Joule heating current during thermal annealing. These parameters could be quantitatively controlled if the linear coherency between thermal diffusivity and electrical conductivity is determined. And at the same time, the TET technique can serve as

an effective method to characterize the thermal and electrical performance.

Declaration of competing interest

The authors declare that they have no known competing financial interests or personal relationships that could have appeared to influence the work reported in this paper.

Acknowledgements

Support of this work by the National Science Foundation (CBET1930866 and CMMI2032464 for X.W.), National Natural Science Foundation of China (No. 51776142 for D.X. and No. 52076156 for Y.Y.) and China Scholarship Council (No. 201906270144 for J.G.) is gratefully acknowledged.

Appendix A. Supplementary data

Supplementary data to this article can be found online at https://doi.org/10.1016/j.carbon.2021.02.102.

References

[1] S.M. Hollen, J.A. Gupta, Painting magnetism on a canvas of graphene, Science 352 (6284) (2016) 415–416.
[2] J.H. Seol, I. Jo, A.L. Moore, L. Lindsay, Z.H. Aitken, M.T. Pettes, X. Li, Z. Yao, R. Huang, D. Broido, Two-dimensional phonon transport in supported graphene, Science 328 (5975) (2010) 213–216.
[3] A.A. Balandin, S. Ghosh, W. Bao, I. Calizo, D. Teweldebrhan, F. Miao, C.N. Lau, Superior thermal conductivity of single-layer graphene, Nano Lett. 8 (3) (2008) 902–907.
[4] S. Chen, A.L. Moore, W. Cai, J.W. Suk, J. An, C. Mishra, C. Amos, C.W. Magnuson, J. Kang, L. Shi, Raman measurements of thermal transport in suspended monolayer graphene of variable sizes in vacuum and gaseous environments, ACS Nano 5 (1) (2011) 321–328.
[5] M.S. Cao, X.X. Wang, W.Q. Cao, J. Yuan, Ultrathin graphene: electrical properties and highly efficient electromagnetic interference shielding, J. Mater. Chem. C 3 (26) (2015) 6589–6599.
[6] W. Lee, J.U. Lee, B.M. Jung, J.H. Byun, J.W. Yi, S.B. Lee, B.S. Kim, Simultaneous enhancement of mechanical, electrical and thermal properties of graphene oxide paper by embedding dopamine, Carbon 65 (2013) 296–304.
[7] T. Schwamb, B.R. Burg, N.C. Schirmer, D. Poulikakos, An electrical method for the measurement of the thermal and electrical conductivity of reduced graphene oxide nanostructures, Nanotechnology 20 (40) (2009) 405704.
[8] C. Deng, C. Li, P. Wang, X. Wang, L. Pan, Revealing the linear relationship between electrical, thermal, mechanical and structural properties of carbon nanocoils, Phys. Chem. Chem. Phys. 20 (19) (2018) 13316–13321.
[9] J. Liu, T. Wang, S. Xu, P. Yuan, X. Xu, X. Wang, Thermal conductivity of giant mono-to few-layered CVD graphene supported on an organic substrate, Nanoscale 8 (19) (2016) 10298–10309.
[10] H. Xie, H. Gu, M. Fujii, X. Zhang, An experimental study on thermal and electrical properties of packed carbon nanofibers, Int. J. Thermophys. 27 (1) (2006) 244–257.
[11] F.G. Emmerich, Young's modulus, thermal conductivity, electrical resistivity and coefficient of thermal expansion of mesophase pitch-based carbon fibers, Carbon 79 (2014) 274–293.
[12] L. Qiu, X. Wang, D. Tang, X. Zheng, P.M. Norris, D. Wen, J. Zhao, X. Zhang, Q. Li, Functionalization and densification of inter-bundle interfaces for improvement in electrical and thermal transport of carbon nanotube fibers, Carbon 105 (2016) 248–259.
[13] B.S. Lee, Thermal conductivity and scattering models for graphene: from intrinsic scattering of pristine graphene to strong extrinsic scattering of functionalized graphene, Appl. Surf. Sci. 497 (2019) 143739.
[14] F. Giannazzo, S. Sonde, R.L. Nigro, E. Rimini, V. Raineri, Mapping the density of scattering centers limiting the electron mean free path in graphene, Nano Lett. 11 (11) (2011) 4612–4618.
[15] A.W. Cummings, D.L. Duong, V.L. Nguyen, D. Van Tuan, J. Kotakoski, J.E. Barrios Vargas, Y.H. Lee, S. Roche, Charge transport in polycrystalline graphene: challenges and opportunities, Adv. Mater. 26 (30) (2014) 5079–5094.
[16] G. Fugallo, A. Cepellotti, L. Paulatto, M. Lazzeri, N. Marzari, F. Mauri, Thermal conductivity of graphene and graphite: collective excitations and mean free paths, Nano Lett. 14 (11) (2014) 6109–6114.
[17] T. Ma, Z. Liu, J. Wen, Y. Gao, X. Ren, H. Chen, C. Jin, X.-L. Ma, N. Xu, H.-M. Cheng, W. Ren, Tailoring the thermal and electrical transport properties of graphene films by grain size engineering, Nat. Commun. 8 (1) (2017) 14486.
[18] T. Rath, P.P. Kundu, Reduced graphene oxide paper based nanocomposite materials for flexible supercapacitors, RSC Adv. 5 (34) (2015) 26666–26674.
[19] N.D.K. Tu, J. Choi, C.R. Park, H. Kim, Remarkable conversion between n- and p-type reduced graphene oxide on varying the thermal annealing temperature, Chem. Mater. 27 (21) (2015) 7362–7369.
[20] J. Guo, X. Wang, T. Wang, Thermal characterization of microscale conductive and nonconductive wires using transient electrothermal technique, J. Appl. Phys. 101 (6) (2007), 063537.
[21] J. Gao, C. Meng, D. Xie, C. Liu, H. Bao, B. Yang, M. Li, Y. Yue, Temperature dependent thermal transport in graphene paper above room temperature, Appl. Therm. Eng. 150 (2019) 1252–1259.
[22] Y. Xie, T. Wang, B. Zhu, C. Yan, P. Zhang, X. Wang, G. Eres, 19-Fold thermal conductivity increase of carbon nanotube bundles toward high-end thermal design applications, Carbon 139 (2018) 445–458.
[23] Z. Xu, X. Wang, H. Xie, Promoted electron transport and sustained phonon transport by DNA down to 10 K, Polymer 55 (24) (2014) 6373–6380.
[24] J. Liu, T. Wang, S. Xu, P. Yuan, X. Xu, X. Wang, Thermal conductivity of giant mono- to few-layered CVD graphene supported on an organic substrate, Nanoscale 8 (19) (2016) 10298–10309.
[25] Y. Xie, P. Yuan, T. Wang, N. Hashemi, X. Wang, Switch on the high thermal conductivity of graphene paper, Nanoscale 8 (40) (2016) 17581–17597.
[26] G. Liu, Q. Tan, H. Kou, L. Zhang, J. Wang, W. Lv, H. Dong, J. Xiong, A flexible temperature sensor based on reduced graphene oxide for robot skin used in internet of things, Sensors 18 (5) (2018) 1400.
[27] J. Campos-Delgado, Y.A. Kim, T. Hayashi, A. Morelos-Gómez, M. Hofmann, H. Muramatsu, M. Endo, H. Terrones, R.D. Shull, M.S. Dresselhaus, M. Terrones, Thermal stability studies of CVD-grown graphene nanoribbons: defect annealing and loop formation, Chem. Phys. Lett. 469 (1) (2009) 177–182.
[28] K. Jia, Y. Su, Y. Chen, J. Luo, J. Yang, P. Lv, Z. Zhang, H. Zhu, C. Zhao, T. Ye, Effects of defects and thermal treatment on the properties of graphene, Vacuum 116 (2015) 90–95.
[29] J. Bai, Y. Huang, Fabrication and electrical properties of graphene nanoribbons, Mat. Sci. Eng. R. 70 (3) (2010) 341–353.
[30] X. Lin, X. Shen, X. Sun, X. Liu, Y. Wu, Z. Wang, J. Kim, Graphene oxide papers simultaneously doped with Mg2+ and Cl− for exceptional mechanical, electrical, and dielectric properties, ACS Appl. Mater. Interfaces 8 (3) (2016) 2360–2371.
[31] J.D. Renteria, S. Ramirez, H. Malekpour, B. Alonso, A. Centeno, A. Zurutuza, A.I. Cocemasov, D.L. Nika, A.A. Balandin, Strongly anisotropic thermal conductivity of free-standing reduced graphene oxide films annealed at high temperature, Adv. Funct. Mater. 25 (29) (2015) 4664–4672.
[32] M. Hu, J. He, Z. Zhao, T.A. Strobel, W. Hu, D. Yu, H. Sun, L. Liu, Z. Li, M. Ma, Y. Kono, J. Shu, H. Mao, Y. Fei, G. Shen, Y. Wang, S.J. Juhl, J.Y. Huang, Z. Liu, B. Xu, Y. Tian, Compressed glassy carbon: an ultrastrong and elastic interpenetrating graphene network, Sci. Adv. 3 (6) (2017), e1603213.
[33] R. Wang, H. Zobeiri, H. Lin, W. Qu, X. Bai, C. Deng, X. Wang, Anisotropic thermal conductivities and structure in lignin-based microscale carbon fibers, Carbon 147 (2019) 58–69.
[34] H. Zobeiri, R. Wang, T. Wang, H. Lin, C. Deng, X. Wang, Frequency-domain energy transport state-resolved Raman for measuring the thermal conductivity of suspended nm-thick $MoSe_2$, Int. J. Heat Mass Tran. 133 (2019) 1074–1085.
[35] C. Li, S. Xu, Y. Yue, B. Yang, X. Wang, Thermal characterization of carbon nanotube fiber by time-domain differential Raman, Carbon 103 (2016) 101–108.
[36] D. Van Tuan, J. Kotakoski, T. Louvet, F. Ortmann, J.C. Meyer, S. Roche, Scaling properties of charge transport in polycrystalline graphene, Nano Lett. 13 (4) (2013) 1730–1735.
[37] F. Gargiulo, O.V. Yazyev, Topological aspects of charge-carrier transmission across grain boundaries in graphene, Nano Lett. 14 (1) (2014) 250–254.
[38] H. Zhang, G. Lee, C. Gong, L. Colombo, K. Cho, Grain boundary effect on electrical transport properties of graphene, J. Phys. Chem. C 118 (5) (2014) 2338–2343.
[39] A. Iskandar, A. AbouKhalil, M. Kazan, W. Kassem, S. Volz, On the interplay between phonon-boundary scattering and phonon-point-defect scattering in SiGe thin films, J. Appl. Phys. 117 (12) (2015) 125102.
[40] Y. Zeng, T. Li, Y. Yao, T. Li, L. Hu, A. Marconnet, Thermally conductive reduced graphene oxide thin films for extreme temperature sensors, Adv. Funct. Mater. 29 (27) (2019) 1901388.
[41] W. Zeng, X. Tao, S. Lin, C. Lee, D. Shi, K. Lam, B. Huang, Q. Wang, Y. Zhao, Defect-engineered reduced graphene oxide sheets with high electric conductivity and controlled thermal conductivity for soft and flexible wearable thermoelectric generators, Nano Energy 54 (2018) 163–174.
[42] D.T. Dias, V.C. Bedeschi, A. Ferreira da Silva, O. Nakamura, M.V. Castro Meira, V.J. Trava-Airoldi, Photoacoustic spectroscopy and thermal diffusivity measurement on hydrogenated amorphous carbon thin films deposited by plasma-enhanced chemical vapor deposition, Diam. Relat. Mater. 48 (2014) 1–5.
[43] H. Lin, S. Xu, X. Wang, N. Mei, Thermal and electrical conduction in ultrathin metallic films: 7 nm down to sub-nanometer thickness, Small 9 (15) (2013) 2585–2594.
[44] E.T. Swartz, R.O. Pohl, Thermal resistance at interfaces, Appl. Phys. Lett. 51 (26) (1987) 2200–2202.
[45] H. Badenhorst, Impact of crystallinity on relationship between electrical and thermal conductivities in bulk graphitic materials, Int. J. Thermophys. 40 (5) (2019) 52.

[46] H. Badenhorst, Optimising graphite composites and plate heat exchangers for latent thermal energy storage using measurements and simulation, J. Energy Storage 29 (2020) 101347.
[47] C. Deng, T. Cong, Y. Xie, R. Wang, T. Wang, L. Pan, X. Wang, In situ investigation of annealing effect on thermophysical properties of single carbon nanocoil, Int. J. Heat Mass Tran. 151 (2020) 119416.
[48] L. Peng, Z. Xu, Z. Liu, Y. Guo, P. Li, C. Gao, Ultrahigh thermal conductive yet superflexible graphene films, Adv. Mater. 29 (27) (2017) 1700589.
[49] G. Xin, T. Yao, H. Sun, S.M. Scott, D. Shao, G. Wang, J. Lian, Highly thermally conductive and mechanically strong graphene fibers, Science 349 (6252) (2015) 1083.
[50] V.B. Mohan, L. Jakisch, K. Jayaraman, D. Bhattacharyya, Role of chemical functional groups on thermal and electrical properties of various graphene oxide derivatives: a comparative x-ray photoelectron spectroscopy analysis, Mater. Res. Express 5 (3) (2018), 035604.
[51] D. Zhang, Z. Shao, D. Geng, X. Jiang, Y. Liu, Z. Zhou, S. Li, Feasibility study of wave-motion milling of carbon fiber reinforced plastic holes, International Journal of Extreme Manufacturing 3 (1) (2020), 010401.
[52] Z. Ahmadi, B. Yakupoglu, N. Azam, S. Elafandi, M. Mahjouri-Samani, Self-limiting laser crystallization and direct writing of 2D materials, International Journal of Extreme Manufacturing 1 (1) (2019), 015001.
[53] P.N. Nirmalraj, T. Lutz, S. Kumar, G.S. Duesberg, J.J. Boland, Nanoscale mapping of electrical resistivity and connectivity in graphene strips and networks, Nano Lett. 11 (1) (2011) 16–22.
[54] H. Wang, S. Hu, K. Takahashi, X. Zhang, H. Takamatsu, J. Chen, Experimental study of thermal rectification in suspended monolayer graphene, Nat. Commun. 8 (1) (2017) 15843.
[55] X. Zhang, S. Fujiwara, M. Fujii, Measurements of thermal conductivity and electrical conductivity of a single carbon fiber, Int. J. Thermophys. 21 (4) (2000) 965–980.